Three-Phase Fractional-Flow Theory of Foam-Oil Displacement in Porous Media with Multiple Steady States

Tang, Jinyu; Castañeda, Pablo; Marchesin, Dan; Rossen, Bill

Important note
To cite this publication, please use the final published version (if applicable).
Please check the document version above.

Correspondence to:
J. Tang,
j.tang-4@tudelft.nl

Three-Phase Fractional-Flow Theory of Foam-Oil Displacement in Porous Media With Multiple Steady States

Jinyu Tang[1] [iD], **Pablo Castañeda[2]** [iD], **Dan Marchesin[3]**, and **William R. Rossen[1]** [iD]

[1]Department of Geoscience and Engineering, Delft University of Technology, Delft, Netherlands, [2]Department of Mathematics, ITAM, Mexico City, Mexico, [3]Instituto Nacional de Matemática Pura e Aplicada (IMPA), Rio de Janeiro, Brazil

Abstract Understanding the interplay of foam and nonaqueous phases in porous media is key to improving the design of foam for enhanced oil recovery and remediation of aquifers and soils. A widely used implicit-texture foam model predicts phenomena analogous to cusp catastrophe theory: The surface describing foam apparent viscosity as a function of fractional flows folds backwards on itself. Thus, there are multiple steady states fitting the same injection condition J defined by the injected fractional flows. Numerical simulations suggest the stable injection state among multiple possible states but do not explain the reason. We address the issue of multiple steady states from the perspective of wave propagation, using three-phase fractional-flow theory. The wave-curve method is applied to solve the two conservation equations for composition paths and wave speeds in 1-D foam-oil flow. There is a composition path from each possible injection state J to the initial state I satisfying the conservation equations. The stable displacement is the one with wave speeds (characteristic velocities) all positive along the path from J to I. In all cases presented, two of the paths feature negative wave velocity at J; such a solution does not correspond to the physical injection conditions. A stable displacement is achieved by either the upper, strong-foam state, or lower, collapsed-foam state but never the intermediate, unstable state. Which state makes the displacement depends on the initial state of a reservoir. The dependence of the choice of the displacing state on initial state is captured by a boundary curve.

Plain Language Summary Foam has unique microstructure and reduces gas mobility significantly. Foam injection into geological formations has broad engineering applications: removal of nonaqueous phase liquid contaminants in aquifers and soils, oil displacement in reservoirs, and carbon storage. Key to the success of foam is foam stability in the presence of oil or nonaqueous phase liquid. An experimentally validated foam model describes foam properties as a function of water, oil, and gas saturations. This model predicts that some injected fractional flows of phases correspond to multiple possible injection states with different saturations: strong-foam state with low mobility, intermediate state, and collapsed-foam state with high mobility. We show how to determine the unique displacing state, using three-phase fractional-flow theory and the wave-curve method. A physically acceptable displacing state is the one that gives only positive wave velocities. The choice of the displacing state depends on the initial state; the nature of the dependence is captured by a boundary curve. If the collapsed-foam state makes a displacement, that means ineffective gas-mobility control and, even in the absence of viscous instability, very slow oil displacement. Our findings and approach presented can help to predict the displacing state for a given initial state in geological formations.

1. Introduction

Catastrophe theory, initially founded by Thom in 1960s and further developed by Zeeman in 1970s, is a branch of bifurcation theory for dynamical systems and of singularity theory in geometry (Arnold et al., 1999; Thom & Zeeman, 1974; Wiggins, 2013; Zeeman, 1977). The cusp catastrophe, among the seven elementary catastrophes described by Zeeman (1977), is schematically illustrated in Figures 1 and 2. The theory of cusp catastrophe states that equilibrium behavior controlled by two independent quantities forms a smooth surface folding on itself. Theoretically, all states between the two edges of the fold in Figure 1 are unstable and cannot be observed in nature. At each edge of the fold, the system makes a sudden and dramatic jump between the two states, illustrated in Figure 2, upon a small change of the controls.
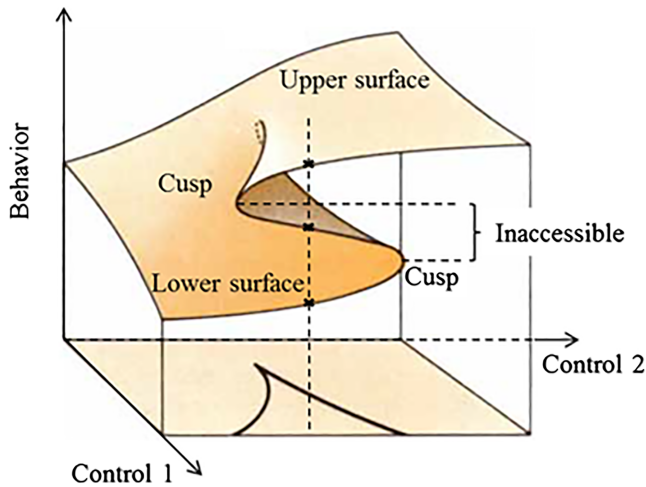
Figure 1. (left) Illustration of the cusp catastrophe: a smooth surface describes behavior at equilibrium as a function of two independent controls; adapted from Zeeman (1977).

In principle, any event meeting the conditions of the theory would exhibit behavior similar to that in Figures 1 and 2. This is found in many models in physics and engineering, for example, in wave propagation, minimum surface area, nonlinear oscillations, and elasticity (Golubitsky & Keyfitz, 1980; Guckenheimer, 1986; Holmes & Rand, 1976; Kravtsov & Orlov, 1990, Purohit & Bhattacharya, 2003). Some theoretical predictions have been verified experimentally or in practice, with others not yet observed. Tang, Ansari, and Rossen (2019) find similar phenomena for foam flow with oil in porous media. Specifically, the widely used foam simulation model in STARS (Computer Modeling Group (Calgary, Alberta, Canada), 2015) predicts, for some combinations of oil, water, and gas fractional flow, three different sets of saturations. Tang, Vincent-Bonnieu, and Rossen (2019) show that this model gives realistic representation of steady state foam behavior with oil. Either this simulator or a foam model similar to that in the simulator has been used to represent a variety of coreflood studies and field applications of foam (Alcorn et al., 2018; Chalbaud et al., 2002; Ma et al., 2013; Norris et al., 2014; Rognmo et al., 2018; Sharma et al., 2017; Spirov et al., 2012). Thus, it is essential to understand the model's behavior, including how it represents displacements with multiple possible displacing states. The study here presents physical insights into these phenomena and their implications for the dynamics of oil displacement by foam.

Numerous processes involve foam flow through porous media, for example, oil displacement in reservoirs (Rossen, 1996; Kovscek et al., 1997; Li et al., 2010), removal of nonaqueous phase liquid contaminants in aquifers and soils (Geistlinger et al., 2009; Jeong & Corapcioglu, 2005; Johnson et al., 2001; Kao et al., 2008) and CO_2 storage (Adebayo, 2018; Adebayo, 2019; Iglauer, Paluszny, et al., 2011; Iglauer, Wülling, et al., 2011; Juanes et al., 2006, Vitoonkijvanich et al., 2015). Foam is not a separate phase but a dispersion of gas in liquid such that gas bubbles are separated by interconnected liquid films, called lamellae. The applications above mainly rely on the fact that foam can reduce gas mobility considerably by trapping gas bubbles via those lamellae (Rossen, 1996). Most oils are detrimental to foam, and this affects significantly the effectiveness of foam for gas mobility control. The interaction between foam and oil is complex and is not yet fully understood (Farajzadeh et al., 2012).

Currently, there exist two groups of models describing foam dynamics in porous media: population-balance models (Kam & Rossen, 2003; Kovscek et al., 1995) and implicit-texture (IT) models (Cheng et al., 2000; Computer Modeling Group (Calgary, Alberta, Canada), 2015). The two groups of models capture different physics involving foam generation and destruction as well as foam behavior at steady state (Lotfollahi et al., 2016).

Population-balance foam models capture the dynamics of foam generation and destruction through a dynamic calculation of bubble density (number of bubbles per unit volume). In the absence of oil, the model of Kam and Rossen (2003) predicts behavior analogous to the cusp catastrophe of Figure 2, where pressure gradient ∇p is plotted as a function of gas (u_g) and water (u_w) superficial velocities (Afsharpoor et al., 2010; Kam & Rossen, 2003). This behavior has been experimentally confirmed in foam corefloods in two ways: first, by showing a sudden jump in ∇p upon a small increase in superficial velocity and, thereafter, a hysteresis with the velocity decreasing; second, in experiments with ∇p fixed, by revealing the entire S-shaped curve illustrated in Figure 2 (Gauglitz et al., 2002). Nevertheless, few current population-balance models represent the effect of oil on foam. The model of Myers and Radke (2000) accounts for the effect of oil by reducing bubble-generation rate in that oil occupies part of pore space and reduces the number of sites where lamellae could be created. This model does not capture the impact of oil on foam stability (e.g., oil condition for foam collapse). Ma et al. (2018) in a recent study
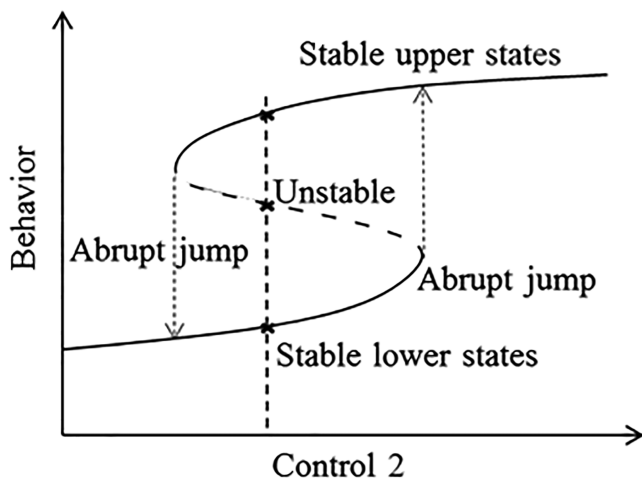

Figure 2. (right) Equilibrium behavior with control 1 fixed on the front plane of Figure 1. Dotted line shows a case of multiple steady states corresponding to the same values of both controls.
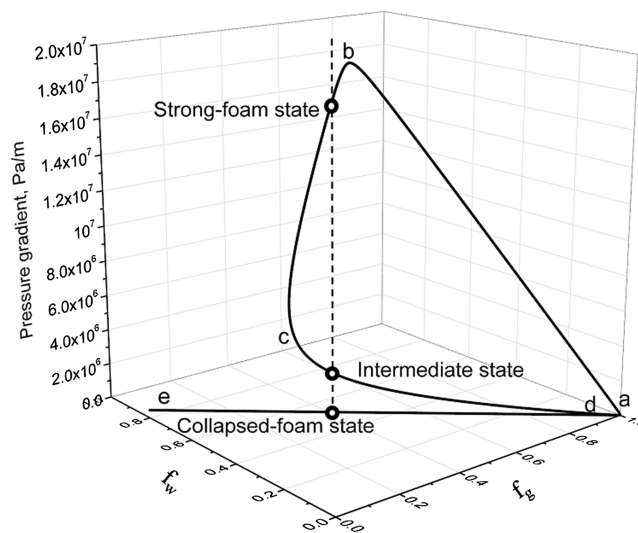
Figure 3. Pressure gradient ∇p as a function of water (f_w) and gas (f_g) fractional flows at total superficial velocity $u_t = 3.53 \times 10^{-5}$ m/s, predicted by the wet-foam representation in Appendix A with a fixed ratio of (f_o/f_w) = 0.25; adapted from Tang, Ansari, and Rossen (2019). The trace follows a sequence: a–e. The dashed line indicates a case of multiple steady states fitting same set of fractional flows, caused by the portion of the curve between c and d folding toward the lower right corner. Model parameters used for the illustration are referred to Table A1 in Appendix A.

attempt to represent the effect of oil by increasing bubble destruction rate in a population-balance model. In separate ways, that model would be expected to alter the low- and high-quality foam regimes, respectively, in a way similar to that of the model described below. The details of behavior of their model and the validity of the model to represent foam flow with oil is not yet experimentally justified.

IT models assume local equilibrium, meaning that foam everywhere immediately reaches a state where bubble generation rate matches destruction rate. Foam texture, that is, bubble size, is not represented explicitly in IT models but is reflected implicitly through a gas mobility-reduction factor. The IT foam model in the STARS simulator defines gas mobility in foam as a function of water (S_w) and oil (S_o) saturations (i.e., fraction of pore volume occupied by water or oil). The approximations of local equilibrium and implicit texture simplify the analysis of foam flow dynamics, in particular in a complex interaction with oil. The model and parameters used below are based on a fit of model parameters to foam behavior without oil (Cheng et al., 2000) and is consistent with foam behavior with oil reported by Tang, Vincent-Bonnieu, and Rossen (2019).

A modeling study by Tang, Vincent-Bonnieu, and Rossen (2019) using the STARS foam model suggests the behavior illustrated in Figures 1 and 2, for steady state foam flow with oil. The behavior was evaluated through foam apparent viscosity μ_{app}, that is, the inverse of total relative mobility (see *Foam Model* section below for its specific definition). With oil, μ_{app} predicted by the model, when plotted on a ternary diagram of oil, water, and gas fractional flows, appears as a surface folding on itself. Figure 3 illustrates this behavior in terms of ∇p as a function of fractional flows, with more details given in the Foam Model section in terms of μ_{app}. The folded region means that, as in Figure 3, there are three possible steady states (associated with different saturations), which fit the same injection condition J defined by a given set of fractional flows. The middle state is intrinsically unstable and therefore not seen in nature. The existence of multiple steady states has not been directly confirmed in the laboratory, but it is physically plausible and consistent with observations of foam behavior (Tang et al., 2018). At the same injection rates, a strong foam, with large μ_{app} and ∇p, might displace oil, resulting in a low oil saturation and thus stable foam; nevertheless, a collapsed foam state with low μ_{app} and ∇p might leave oil saturation high and foam unstable. This raises an essential question concerning the effectiveness of foam displacements: Which of the multiple steady states, with different μ_{app} and ∇p, all fitting to a same set of injected fractional flows, actually occurs in a given displacement?

Tang , Ansari, and Rossen (2019) performed simple 1-D numerical simulations with fixed injection rates corresponding to cases with multiple possible states. Their simulation results suggest a displacement by either the upper state, with large μ_{app}, or the lower state, with small μ_{app}, but never the (unstable) one in the

middle. These observations are consistent with catastrophe theory. However, a numerical simulation does not explain why a particular (strong or weak) foam is seen in the displacement.

We here present an analysis of a displacement with multiple possible injection states fitting the same injected fractional flows, using an analytical approach, the wave curve method (WCM) for three-phase flow. The WCM is also referred to, in petroleum engineering, as fractional-flow theory or the method of characteristics. Fractional-flow theory excludes the numerical artifacts that can afflict foam simulation (Rossen, 2013).

A computer-assisted design package, RPn (*n*-dimensional Riemann Problem) that applies the WCM has been developed in the group of fluid dynamics at IMPA (Instituto Nacional de Matemática Pura e Aplicada) in Brazil (Azevedo et al., 2010; Castañeda et al., 2016). This program efficiently determines Riemann solutions for 1-D three-phase flow, including the complications of foam. The Riemann solutions provide a mathematical criterion that distinguishes states observed or not observed in the displacement. Using this tool, we explore the dependence of the displacement on initial condition.

The significance of our findings for field applications is discussed below. Some suggestions are provided for the direct experimental verification of multiple steady states through foam corefloods in laboratory.

2. Theory and Mathematical Approach

2.1. Three-Phase Fractional-Flow Theory

The core of fractional-flow theory concerns modeling transport of fluids in porous media, specifically, by solving for phase saturations as a function of position x and time t (Lake et al., 2014). The solutions are usually illustrated as a saturation profile as a function of position at a given time or saturation history at a given position.

In a system of foam flow with oil, the presence of three phases means there are two independent variables to be determined, water (S_w) and oil (S_o) saturations as functions of (x, t). Gas saturation is $S_g = (1 - S_w - S_o)$. For the purpose of our study, we have made the following assumptions:

1. 1-D flow in a homogeneous porous medium. The model does not represent fingering that would occur in 2-D or 3-D, but it does identify regions or fronts with viscous instability where fingering would be likely.
2. incompressible fluids and rock,
3. immediate attainment of local-equilibrium behavior,
4. no dispersive processes (diffusion, dispersion, or flow driven by capillary-pressure gradients),
5. gravity can be ignored,
6. no mass exchange between phases (immiscible phases),
7. isothermal process,
8. Newtonian rheology for all phases, and
9. uniform concentration of surfactant in the aqueous phase throughout the medium, which implies that adsorption has already been satisfied.

The local-equilibrium assumption means that foam generation and destruction rates come to equilibrium instantaneously. In local-equilibrium modeling of a displacement, this assumption means foam at any location is modeled as a function of local phase saturations. This approximation is justified by foam-displacement experiments without oil (e.g., Kovscek et al., 2010) and by simulations in which such effects are explicitly introduced (Kam et al., 2007).

Capillary diffusion (flow driven by local gradients of capillary pressure) is modeled as a function of saturations, which affects phase distributions in a displacement. Multiple steady states as represented by the model in Appendix A are a result of combined effects of S_w and S_o (Tang et al., 2019). With or without localized capillary diffusion, in a sufficiently long displacement, there are some combinations of S_w and S_o in ternary saturation space that correspond to different foam viscosities but the same fractional flows. The existence of the multiple steady states is, therefore, independent of capillary diffusion.

With foam, gas mobility can be reduced by a factor, for example, of thousands (Tang, Vincent-Bonnieu, & Rossen, 2019). Compared to viscous forces in foam injection, gravitational forces are negligibly small. That is supported by CT foam corefloods where saturations are measured (e.g., Simjoo et al., 2013; Tang, 2019).

The modeling of foam-oil flow described below assumes a homogeneous porous medium. Some other physical factors not considered here include formation heterogeneity, surfactant adsorption, gradients of capillary pressure, and gravity separation. These would greatly complicate conditions in geological formations for foam generation and/or propagation. For instance, Shah et al. (2018) experimentally show that low-to-high permeability boundaries assist in foam generation through capillary snap-off. Al Ayesh et al. (2017) in a modeling analysis show that permeability affects foam stability and strength, thus resulting in diversion of flow from high to low permeability layers. Our goal is first to understand behavior in a simplified system before extending the analysis to these complications.

The system is governed by two mass-conservation equations for $x > 0$ and $t > 0$:

$$\varphi \frac{\partial S_w}{\partial t} + u \frac{\partial f_w}{\partial x} = 0, \tag{1}$$

$$\varphi \frac{\partial S_o}{\partial t} + u \frac{\partial f_o}{\partial x} = 0, \tag{2}$$

where φ is porosity, a rock property (a volume fraction of rock that is pore space) and u is the total superficial velocity of the three phases, that is, $u \equiv u_w + u_o + u_g$. f_w and f_o in equations (1) and (2) are the fractional flows of water and oil, defined as the fraction of phase volumetric flux to the total volumetric flux:

$$f_j \equiv \frac{u_j}{u}, \tag{3}$$

where subscript $j = w$, o, or g represents water, oil, or gas, respectively.

Superficial velocity u_j of phase j is determined by Darcy's law:

$$u_j = \frac{k k_{rj}}{\mu_j} |\nabla p|, \tag{4}$$

where k is the absolute permeability of the porous medium, μ_w, μ_o, and μ_g are the water, oil, and gas viscosities, $|\nabla p|$ is the absolute magnitude of pressure gradient, and k_{rj} is the relative permeability of phase j. The ratio of (k_{rj}/μ_j) is referred to as the relative mobility of phase j.

Substituting equation (4) into equation (3) yields

$$f_j = \frac{k_{rj}/\mu_j}{k_{rw}/\mu_w + k_{ro}/\mu_o + k_{rg}^f/\mu_g}, \tag{5}$$

where superscript f in k_{rg}^f indicates the presence of foam. We assume that presence of foam does not alter the relative-permeability function for water or oil but only that for gas. This is supported by a number of experimental observations and greatly simplifies the physics and modeling of foam flow in porous media (Rossen, 1996; Schramm, 1994).

In the STARS foam model (see Appendix A for specific algorithms), k_{rg}^f with foam is defined as foam-free gas relative permeability, k_{rg} reduced by a mobility-reduction factor *FM* (Computer Modeling Group (Calgary, Alberta, Canada), 2015). The scaling factor *FM*, given in equation (A2) in Appendix A, is a function of a series of physical factors affecting foam stability and degree of gas-mobility reduction by foam. Two major factors in *FM* concerning water and oil saturations are included in this study, meaning that *FM* is a function only of saturations.

The commonly used models for k_{rj} include Stone I and II (Stone, 1970, 1973) and the Corey model. In a case of three-phase flow, k_{rj} of the intermediate-wetting phase in Stone I and II is related to that of the other two phases based on channel-flow theory, rather than a unique function of its own saturation. Foam alters gas mobility so drastically that Stone's models can give unphysical results with foam, for example, positive relative permeability at zero oil saturation. For simplicity, therefore, we use a Corey-type relative-permeability model, where k_{rj} of phase j without foam is a function of S_j alone:

$$k_{rj} = k_{rj}^0 \left(\frac{S_j - S_{jr}}{1 - S_{wc} - S_{or} - S_{gr}} \right)^{n_j}, \tag{6}$$

where k_{rj}^0 is the endpoint relative permeability, n_j is the Corey exponent that reflects wettability, and S_{wc}, S_{or}, and S_{gr} represent the residual saturations of each phase. Equation (A2) in Appendix A for *FM*, with F_2 and F_3 included, combined with equation (6) for k_{rj}, suggest that fractional flow f_j in equation (5) is a function only of saturations.

To simplify equations (1) and (2), dimensionless position, x_D, and time, t_D are introduced:

$$x_D \equiv \frac{x}{L}, \tag{7}$$

$$t_D \equiv \frac{u \cdot t}{(1 - S_{wc} - S_{gr} - S_{or}) L \varphi}, \tag{8}$$

where L is the 1-D reservoir length and t_D is the number of movable pore volumes injected, with movable pore volume scaled by $(1 - S_{wc} - S_{gr} - S_{or})$. Equations (1) and (2) then are simplified to

$$\frac{\partial S}{\partial t_D} + \frac{\partial F}{\partial x_D} = 0, \tag{9}$$

where S and F are both vectors, that is, $S = \begin{pmatrix} S_w \\ S_o \end{pmatrix}$ and $F = \begin{pmatrix} f_w \\ f_o \end{pmatrix}$.

Fractional-flow theory interprets a displacement process in terms of wave propagation (Avraam & Payatakes, 1995; Buckley & Leverett, 1942; Charbeneau, 1988; Lake et al., 2014; Reynolds & Krevor, 2015; Wooding & Morel-Seytoux, 1976). In principle, all saturations between *J* and *I* along a composition path exist at the origin at $t_D = 0$. Upon injection, water, oil, and gas propagate starting from the origin with given wave speeds as a function of saturations. Solving for the saturation profile and history is then equivalent to solving for waves speeds, $\eta(S)$:

$$\eta(S) \equiv \frac{x_D}{t_D}. \tag{10}$$

Substituting $\eta(S)$ into equation (9) and using chain rule of differentiation, the system is rearranged to (Lake et al., 2014):

$$[J(S) - \eta I^*] dS = 0, \tag{11}$$

where I^* denotes the 2-by-2 identity matrix, with an asterisk to distinguish it from the initial state, *I*. $J(S)$ is the Jacobian matrix:

$$J(S) = \begin{pmatrix} J_{ww}(S) & J_{wo}(S) \\ J_{ow}(S) & J_{oo}(S) \end{pmatrix}, \tag{12}$$

where $J_{ij}(S) = \partial f_i / \partial S_j$ with i and j = w, o, and g denoting water, oil, and gas, respectively.

Mathematically, $\eta(S)$ to be solved is the eigenvalue of the Jacobian matrix $J(S)$. A physical problem of solving for wave speeds, $\eta(S)$, is eventually converted to a mathematical problem concerning eigenvalues of the Jacobian matrix in equation (12) (Castañeda, 2018; Castañeda et al., 2016; Lax, 1957; Liu, 1974).

2.2. Wave-Curve Method

The WCM implemented in the RPn solves the system described by equation (9) for two major outputs: a composition path from *J* to *I* that provides *S* along the path and the associated wave speed for each value of *S*. The two types of solutions together define the structure of a displacement. From the saturations and wave speeds arising from $x_D = t_D = 0$, the saturation profile can be determined at any time and the saturation history at any location. A number of studies of multiphase flow in porous media, concerning a hyperbolic
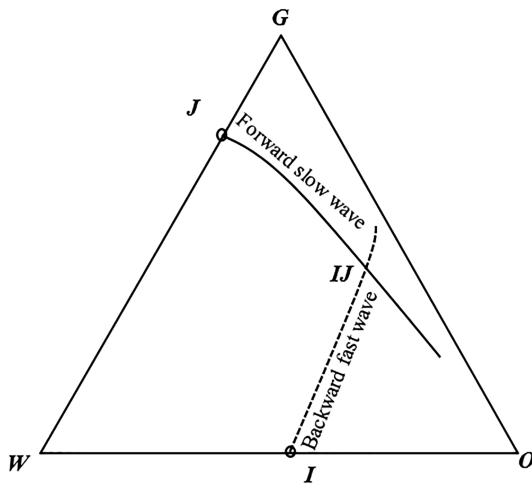
Figure 4. Simplified schematic of wave-curve construction in the RPn program using the wave-curve method. The three vertices G, O, and W represent the saturations of gas, oil, and water, respectively, where only that phase flows: that is, at residual saturation of the other two phases. Thus, residual phase saturations are not shown on this, or subsequent, plots. The slow wave curve is constructed in the forward direction starting from J, and the fast wave curve in the backward direction initiating from I.

system of conservation laws, provide a detailed description of the method (Azevedo et al., 2010; Castañeda, 2018; Castañeda et al., 2016). This section briefly explains the general principles of the WCM applied in the RPn program (Liu, 1974; Smoller, 2012), especially to distinguish the Riemann problem that the WCM solves from that of physical displacements.

Generally, the composition path for J displacing I is determined by constructing two families of wave curves via the WCM, as illustrated in Figure 4: a forward slow-wave curve and a backward fast-wave curve. The forward slow wave curve starts from J; the smaller eigenvalue of J (S) in equation (12) at each saturation is assigned in the WCM as the characteristic speed at saturation S. The corresponding eigenvector gives the direction of saturation change from the current saturation to the next saturation. At this saturation, the eigenvalues of J(S) in equation (12) are again calculated and the process continues until the entire slow path is determined.

Saturations within a shock, if it occurs, are unphysical and do not appear on a saturation profile. That leads to a discontinuity in saturations, meaning that the shock speed cannot be resolved through J(S) comprising derivatives that are a function of saturations. The shock and its speed σ that reach I are then determined by constructing a Rankine-Hugoniot (RH) locus via the RH condition (Azevedo et al., 2010; Castañeda et al., 2016):

$$F(S)-F(S_I) = \sigma(S-S_I), \tag{13}$$

where S_I represent phase saturations at I. The RH condition is derived from a mass balance across a shock. This condition as in equation (13) defines all possible states that may reach I via a shock, seen from the dashed line in Figure 4, referred to as the backward fast-wave curve.

The two families of wave curves as illustrated in Figure 4 cross at some point denoted IJ, at which the slow speed is less than the fast wave speed. The spreading wave velocities of saturations along the forward slow-wave curve increase in the forward direction starting from J. The shock velocities of points, along the backward fast-wave curve, decrease in the backward direction initiating from I to IJ. The whole path, from J to IJ and then to I, is thus guaranteed to meet the compatibility of monotonically increasing wave velocity. This result hinges on the nonlinearity of relative-permeability functions. In the simplified case of linear relative-permeability functions, shocks (equation (13)) occur along the same curve as spreading waves (equation (11)), but this is not the case in general (Lake et al., 2014; Namdar Zanganeh et al., 2011).

To avoid confusion in mathematical and engineering terminologies, we clarify that all the states that connect J to I (solved through the two families of wave curves), as shown in Figure 4 and subsequent illustrations, are referred to as a composition path. Saturation points on a spreading-wave curve are physical, which can be observed in a displacement. The two endpoints of a shock wave (i.e., intersection state IJ and initial state I in Figure 4) are physical and can also be observed, whereas the other saturation points between these two states within the shock are unphysical, which cannot be observed.

Note that the WCM for three-phase flow solves a problem with different constrains than a coreflood with specified injection rates of phases. In a coreflood, at $t_D = 0$, initial state I is defined as follows:

$$\begin{cases} S(x_D, 0) = I & 0 < x_D \leq 1 \\ S(x_D, 0) = J & x_D = 0 \end{cases}. \tag{14}$$

Upon injection, initial state I, present for $0 < x_D \leq 1$, is displaced forward by injection state J starting at $x_D = 0$ with specified fractional flows of phases, as schematically illustrated in Figure 5.
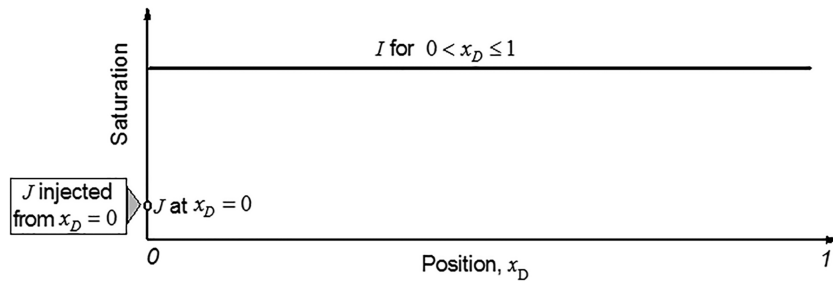
Figure 5. Schematic of problem definition for a coreflood. Injection state J, originating from $x_D = 0$ with given fractional flows of phases, displaces initial state I present for $0 < x_D \leq 1$.

Strictly, the WCM does not specifically solve for a physical displacement of I for $0 < x_D \leq 1$ by J at $x_D = 0$. Instead, as shown in Figure 6, it solves for an initial state with I present for $x_D > 0$ and J for $x_D \leq 0$:

$$\begin{cases} S(x_D, 0) = I & x_D > 0 \\ S(x_D, 0) = J & x_D \leq 0 \end{cases}, \tag{15}$$

where S is a vector of saturations in a case of three-phase flow. Starting at time $t_D = 0$, injection of state J (from $x_D < \; < 0$) begins, and the state evolves. The analysis below shows that this distinction is crucial to determining the correct displacing state J among multiple possible injection states. In particular, only a composition path with all positive wave velocities can represent a physical displacement by J at $x_D = 0$.

3. Foam Model

A key to the success of foam-related applications is the physical stability and strength of foam with oil. We here apply the widely used IT foam model in the STARS simulator (Computer Modeling Group (Calgary, Alberta, Canada), 2015; Cheng et al., 2000). It includes two algorithms describing the effect of oil on foam properties: the wet-foam representation and the dry-out representation. Appendix A gives the wet-foam representation that describes impacts of a series of physical factors on foam properties, that is, surfactant concentration, water saturation, oil saturation, salinity, shear-thinning rheology, and capillary number. Two major functions, in equations (A3) and (A4), are included in this study to quantify the effect of S_w and S_o on foam properties. The dry-out representation (equation (A3)) can also predict multiple steady states (Tang, Ansari, & Rossen, 2019), but we do not employ it here.

The model parameters we used are based on a detailed fit of coreflood data for foam without oil (Alvarez et al., 2001; Cheng et al., 2000) and are consistent with coreflood data on foam with oil (Tang, Vincent-Bonnieu, & Rossen, 2019).

3.1. Foam Representation on Ternary Diagram

In corefloods, the mobility reduction in gas by foam is measured through pressure drop or pressure gradient. In modeling, this is evaluated via a mobility-reduction factor FM (equation (A2) in Appendix A) as a function of S_w and S_o. Through the factor FM, foam modifies gas mobility by reducing gas relative
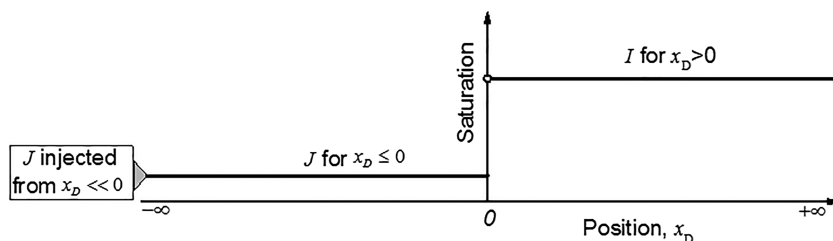

Figure 6. Schematic of problem definition for a displacement solved in the wave-curve method. Injection state J, from $x_D < \; < 0$, drives an initial state of I for $x_D > 0$ and J for $x_D \leq 0$.
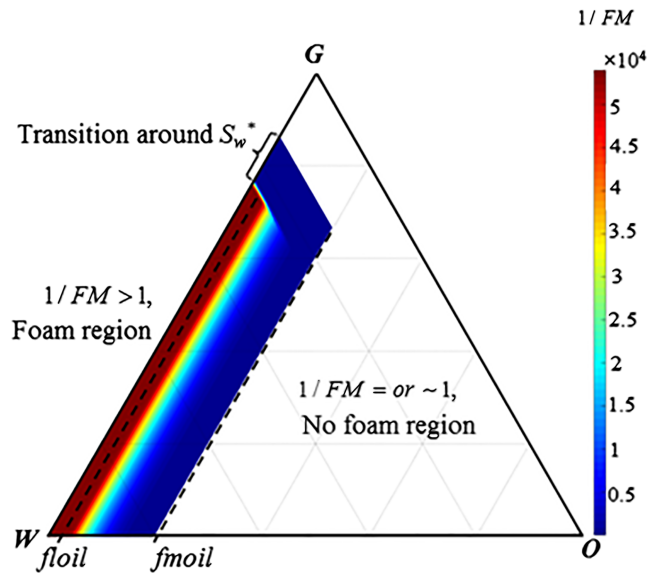
Figure 7. Foam-property map in ternary saturation space, visualized through gas-mobility-reduction factor ($1/FM$) defined by the wet-foam representation. The factor ($1/FM$) is given in equation (A2), with functions F_2 defined in equation (A3) and F_3 defined in equation (A4), accounting for the impacts of S_w and S_o on foam, respectively. Model parameters are in Table A1 in Appendix A.

permeability. A larger value of ($1/FM$) indicates greater reduction to gas mobility and thus stronger foam. The model parameters used as given in Table A1 in Appendix A indicate a very strong foam, with an abrupt collapse of foam at S_w near the limiting water saturation, *fmdry* (physically denoted as S_w^*).

Figure 7 plots ($1/FM$) in equation (A2) in ternary saturation space as defined in the wet-foam representation, where function F_2 in equation (A3), for the effect of S_w, and F_3 in equation (A4), for the effect of S_o, are considered. Generally, the factor ($1/FM$) splits the ternary saturation space into three regions: a full-strength foam region, a partially destabilized foam region, and a no-foam region. The region with foam either at full strength or partially destabilized has ($1/FM$) > 1; this region resides at the lower-left corner of the ternary diagram. The remaining, white region, with ($1/FM$) ~ *1*, indicates absence of foam.

The absence of foam indicated by the white region in Figure 7 arises mainly from two reasons related to foam stability and strength. Foam stability is controlled by the limiting capillary pressure, which corresponds to a limiting water saturation S_w^* (Khatib et al., 1988; Rossen & Zhou, 1995). Along a direction parallel to the G–O binary, for S_w lower than S_w^*, foam collapses. The abruptness of collapse depends on an adjustable parameter *epdry* in equation (A3), the value of which is large in this study as justified in coreflood measurements (Kim et al., 2005; Boeije & Rossen, 2015; Tang et al., 2018). Specifically, for S_w just a bit less than S_w^*, F_2 in equation (A3) is nearly zero, setting the inverse of factor FM in equation (A1) close to unity. There is nearly no reduction in k_{rg}^f due to absence of foam in this range of S_w. As S_w rises, a transition zone in the interval around S_w^*, seen in Figure 7, is marked by an abrupt increase in ($1/FM$). This zone corresponds to an abrupt drop in k_{rg}^f around S_w^* in Figure A1 in Appendix A. For S_w greater than S_w^*, foam is at full strength in the absence of oil.

In the other direction, parallel to the G–W binary, increasing S_o weakens foam via equation (A4), leading to a larger value of FM and thus less gas-mobility reduction. The effect of S_o in equation (A4) is bounded by two limits, an upper-limiting oil saturation *fmoil* and lower-limiting oil saturation *floil*. Specifically, for S_o < *floil*, oil-saturation-dependent function F_3 in equation (A4) equals unity, meaning that oil has no detrimental impact on foam. For S_o between *floil* and *fmoil*, oil shows a nonlinear effect, indicated by the color gradient in Figure 7. When S_o > *fmoil*, F_3 is zero, with ($1/FM$) = 1; foam is killed completely. This corresponds to the sudden rise of k_{rg}^f around S_w, roughly 0.45 along the bottom axis of Figure A1 in Appendix A. The full-strength foam results from combined effects of S_w and S_o, specifically for $S_w > S_{w^*}$ and $S_o < $ *floil*.

3.2. Multiple Steady States in Foam Model

Experimental observations show that most oils destabilize foam (Farajzadeh et al., 2012; Rossen, 1996). The widely used IT foam model shown in Appendix A suggests a cusp catastrophe as in Figures 1 and 2, leading to multiple steady states. Tang, Ansari, and Rossen (2019) provide a detailed analysis of the occurrence of the multiple steady states. These phenomena are briefly described here for the purpose of our study.

The foam properties as shown in Figure 7 are usually evaluated through foam apparent viscosity μ_{app}. A larger value of μ_{app} indicates stronger foam. Treating multiphase flow in foam flow with oil as a pseudo-single phase and applying Darcy's law gives the definition of apparent viscosity, μ_{app}:

$$\mu_{app} \equiv \frac{k|\nabla p|}{u}, \tag{16}$$

where u represents the total superficial velocity. With $u = u_w + u_o + u_g$, solving for ∇p for three-phase flow (equation (4)) and substituting into equation (16) returns μ_{app} as a function of (S_w, S_o):
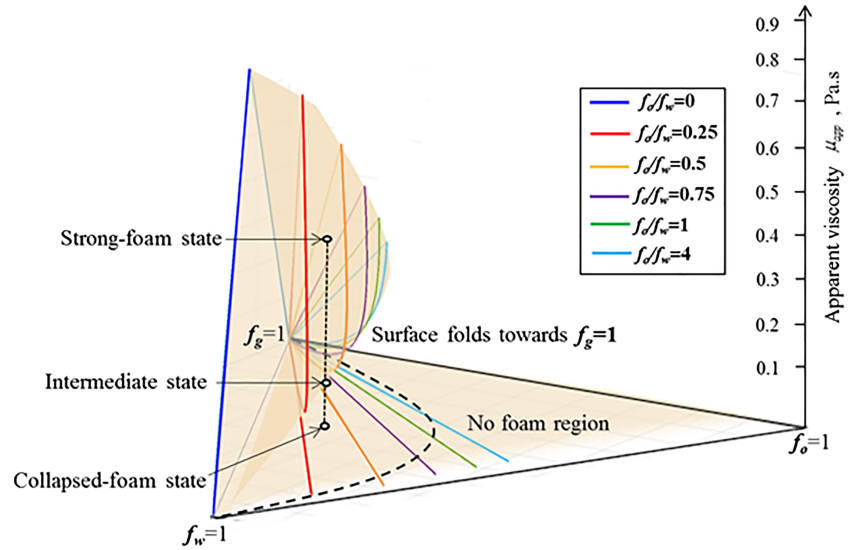
Figure 8. A surface describing foam apparent viscosity μ_{app} as a function of f_w, f_o, and f_g, predicted by the wet-foam representation in Appendix A. The three vertices represent 100% f_w, f_o, and f_g, respectively. The curves on the surface are plotted with various fixed ratios (f_o/f_w). The dashed line on the plane of ternary diagram illustrates projection of the surface. The vertical dashed line indicates a case of multiple steady states fitting a same set of fractional flows: an upper strong-foam state, intermediate state and lower collapsed-foam state.

$$\mu_{app} = \frac{1}{k_{rw}/\mu_w + k_{ro}/\mu_o + k_{rg}^f/\mu_g}, \tag{17}$$

where the denominator $(k_{rw}/\mu_w + k_{ro}/\mu_o + k_{rg}^f/\mu_g)$ is the total relative mobility. Since fractional flows f_j for each phase defined in equation (5) are also functions only of (S_w, S_o), μ_{app} is then correlated to f_g, f_o, and f_w through (S_w, S_o).

Figure 8 plots μ_{app} as a function of f_g, f_o, and f_w, using the wet-foam representation in Appendix A. On a ternary diagram of fractional flows, the shape of foam apparent viscosity μ_{app} forms a surface. The curves on the surface are plotted for μ_{app} at various fixed ratios (f_o/f_w), which is equivalent to fixing (u_o/u_w). The blue curve, along the f_g-f_w binary, shows the changing trend of μ_{app} without oil. As a group, the curves illustrate the shape of the surface.

A key feature illustrated in Figure 8 is that the surface folds back toward $f_g = 1$ in the middle, due to the destabilizing effect of oil on foam, as explained by Tang, Ansari, and Rossen (2019). In the folded region, a set of fractional flows f_g, f_o, and f_w corresponds to three possible steady states: a strong foam state with large μ_{app} on the upper surface, a collapsed foam state with very small μ_{app} at the bottom, nearly flat surface, and the intermediate state on the folding surface. The projection of the folded region onto the ternary diagram gives the dashed line, beyond which foam does not exist, either due to low S_w or high S_o. As briefly mentioned in the section 1, the key issue we answer in the following section is which of the multiple possible steady states is the displacing state to oil for injection with fractional flows in the folded region. The displacing state controls the success of a foam process, since different states have very different mobilities.

4. Displacing State Among Multiple Steady States

For a number of engineering applications described by a cusp catastrophe, the final state achieved in the folded region depends on the initial state (Golubitsky & Keyfitz, 1980; Guckenheimer, 1986; Holmes & Rand, 1976; Kravtsov & Orlov, 1990). For a given set of injected fractional flows, we define two types of initial conditions I, that is, unfavorable (I_1) or favorable (I_2) to displacement by stable foam. Figure 9 gives an example of a set of multiple steady states J_1, J_2, and J_3, all fitting the same injected fractional flows, and two types
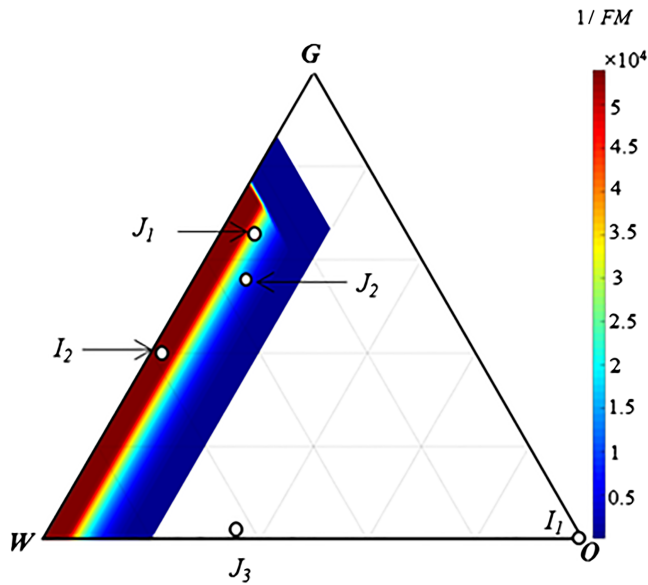
Figure 9. Illustration of a displacement with multiple possible displacing states represented by J_1 (upper state–low mobility), J_2 (middle state), and J_3 (lower state–high mobility) corresponding to the same injected fractional flows. I_1 and I_2 represent two initial conditions, unfavorable and favorable for displacement by stable foam (upper state), respectively. The colored patch indicates the foam region. Saturations are given in Table 1.

of initial states I_1 and I_2. There are thus six composition paths, from each of J_1, J_2, and J_3, to each of I_1, and I_2, respectively. The question is which path represents the solution for the given injected fractional flows and each initial condition.

Table 1 summarizes the saturations of each possible injection state, J_1, J_2, and J_3, and of the two types of initial conditions, I_1 and I_2 in Figure 9. All the parameters needed in the construction of composition paths are taken from Table A1 in Appendix A.

Note that I_1 and I_2 in Figure 9 were selected outside and inside the foam region, to illustrate the impact of the initial state on the choice of the displacing state among J_1 and J_2 and J_3. However, the fundamental division of I in ternary saturation space, for the choice of the displacing state among the given set of J_1, J_2, and J_3, is not necessarily the boundary of the foam region. The dependence of the displacing state on the initial state is captured through a boundary curve shown below.

4.1. Initial State Outside Foam Region

The two major outputs in Riemann solutions solved by the WCM— composition paths and wave speeds—provide physical insights that unravel the occurrence and features of a displacement, that is, wave type, configuration, and propagation. We analyze Scenario 1 in Table 1 first, with the initial state I_1 outside the foam region, based on the Riemann solutions of cases 1, 2, and 3 with J_1, J_2, and J_3 as the injection state, respectively.

Figure 10 shows the three composition paths from each of J_1, J_2, and J_3 to I_1. Though J_2 might be intrinsically unstable as suggested by catastrophe theory, one could still theoretically construct a composition path from J_2 to I_1. Tracks of the three paths from J to I on Figure 10 follow, respectively: J_1–A_1–B_1–C_1–D_1–I_1; J_2–A_2–B_2–C_2–D_2–I_1; J_3–C_3–D_3–I_1. Each path comprises two groups of wave curves, that is, the forward slow-wave group from J and backward fast-wave group from I as schematically illustrated in Figure 4. These two groups of wave curves in a path are distinguished by the intersection state IJ, that corresponds to the point C_1 in J_1 path, C_2 in J_2 path, and C_3 in J_3 path, respectively. Along each path in Figure 10, the portion from J to IJ represents the slow-wave group, and the rest portion from IJ to I corresponds to the fast-wave group.

The specific structure of the three paths in Figure 10 is indicated by dashed and solid curves that represent the shock and spreading waves, respectively. The labelled letters A_k, B_k, C_k, and D_k (k = 1, 2, and 3) indicate the transitions along each path from a shock to a spreading wave or the reverse. The paths from J_1 and J_2 to I_1 exhibit similar wave type and configuration. Both paths start from the injection state with a shock wave (from J_1 to A_1 along the path from J_1 or J_2 to A_2 along the path from J_2) followed by a spreading wave (from A_1 to B_1 or A_2 to B_2). Thereafter, there occurs a second shock (from B_1 to C_1 or B_2 to C_2), that is connected to a second spreading wave (from C_1 to D_1 or C_2 to D_2) which eventually reaches I_1 with a shock, that is, from D_1

Table 1
A Summary of Cases Presented for the Analysis of Multiple Possible Displacing States Fitting the Same Injected Fractional Flows

Scenarios		Injection conditions $J = (S_w, S_o)$		Initial conditions $I = (S_w, S_o)$	Remark
Scenario 1	Case 1	$J_1 = (0.26998, 0.05404)$	Strong foam state	$I_1 = (0, 1)$, outside stable foam region	J_1, J_2, and J_3, all fit the same set of (f_w, f_o, f_g)
	Case 2	$J_2 = (0.36382, 0.10110)$	Intermediate state		
	Case 3	$J_3 = (0.65210, 0.34435)$	Collapsed foam state		
Scenario 2	Case 1	$J_1 = (0.26998, 0.05404)$	Strong foam state	$I_2 = (0.6, 0.01)$, inside stable foam region	
	Case 2	$J_2 = (0.36382, 0.10110)$	Intermediate state		
	Case 3	$J_3 = (0.65210, 0.34435)$	Collapsed-foam state		

Note. All saturations listed here are normalized for residual saturations through equation (A5) in Appendix A.
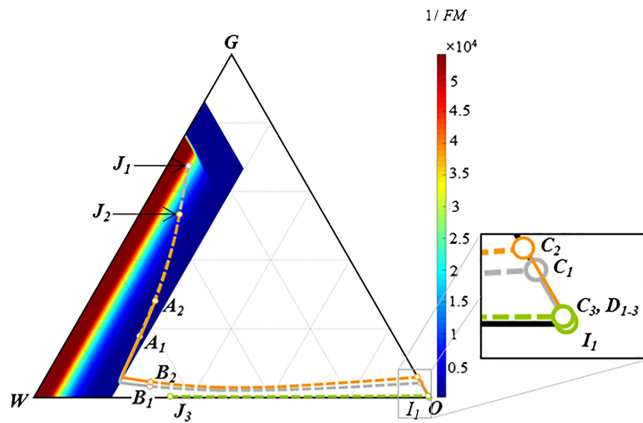
Figure 10. Three composition paths in ternary saturation space constructed from each of J_1, J_2, and J_3, respectively, to I_1, which resides outside the foam region. The respective tracks of the three paths are denoted by: J_1–A_1–B_1–C_1–D_1–I_1; J_2–A_2–B_2–C_2–D_2–I_1; J_3–C_3–D_3–I_1. The three saturation points at J_1, J_2, and J_3 represent three foam states, all fitting the same (f_w, f_o, f_g). A solid curve represents a spreading wave and a dashed curve represents a shock.

to I_1 or D_2 to I_1. Both paths feature a sharp inflection across the foam boundary at $S_o = fmoil$. This arises from foam collapse that yields an abrupt rise in gas mobility. Capturing this sharp inflection in calculations requires very fine resolution in saturation steps. The path from J_3 (with very small gas fractional flow as given in Table 1), at which foam is fully collapsed, starts with a shock from J_3 to C_3. A nearly invisible spreading wave in Figure 10 connects C_3 to D_3, which shocks to I_1.

Figures 11a–11c illustrate trajectories of the associated wave speeds as a function of saturations along each path from J_1, J_2, and J_3 to I_1 in dimensionless x_D versus t_D space. Fractional-flow theory states that, as implied by equation (10) (Lake et al., 2014), the slope of each trajectory line in Figure 11 is the constant wave speed of a given feature (shock, characteristic, etc.). A red trajectory corresponds to a shock wave, as denoted by a dashed curve in Figure 10. Black lines in Figure 11 represent characteristics within spreading waves. I, J, and IJ mark constant-state regions, with IJ being the intersection state at C_1, C_2, or C_3 as illustrated in Figure 4. The existence of the constant-state region at IJ is a major difference between two- and three-phase flows in porous media.

Comparing the wave velocities in Figures 11a–11c shows that the paths from each of J_1 and J_2 to I_1 pass through the bottom quadrant, reflecting negative wave speeds. In a physical displacement, the injected fractional flows $F(J)$ are maintained fixed at $x_D = 0$ as shown in Figure 5. However, for both paths starting from J_1 and J_2 as in Figures 11a and 11b, the fractional flows at $x_D = 0$ with $t_D > 0$ deviate from those at J_1 or J_2, due to the negative wave velocities. The appearance of negative wave velocities then rules out a foam state being the displacing state in a physically acceptable displacement.
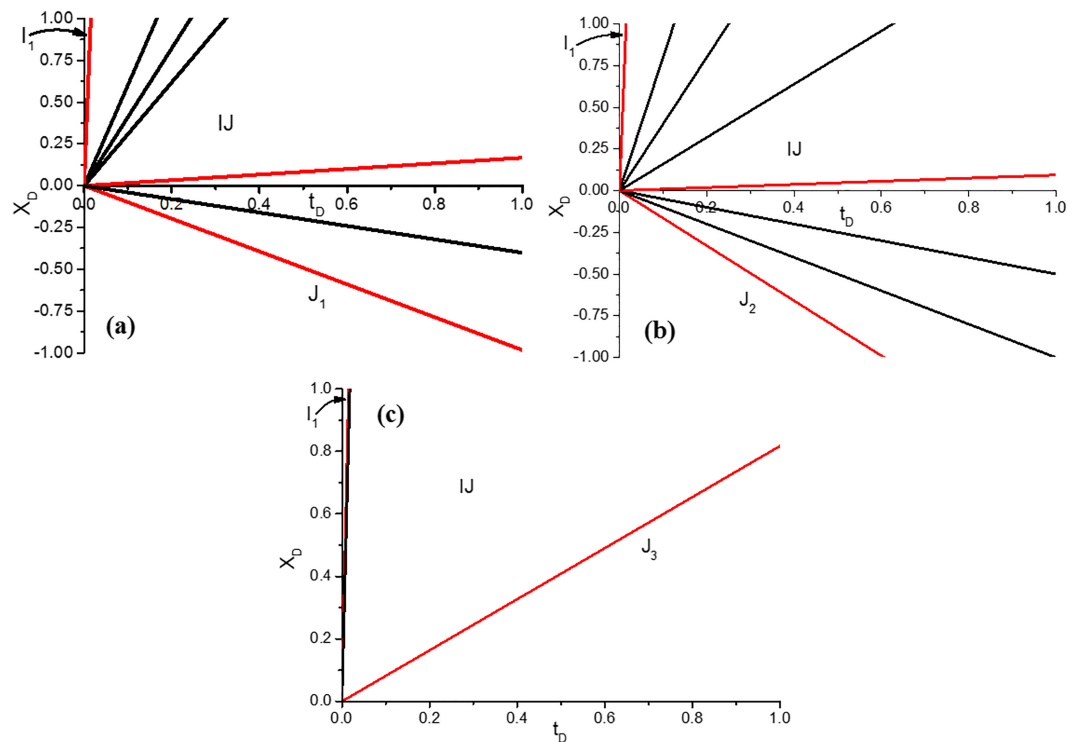

Figure 11. Trajectories of the associated wave speeds as a function of saturations along each path from J_1, J_2, and J_3 to I_1 in Figure 10 in dimensionless x_D versu t_D space. A red trajectory marks a shock, with black lines representing characteristics within spreading waves. Only the path from J_3 gives wave speeds that are all positive.
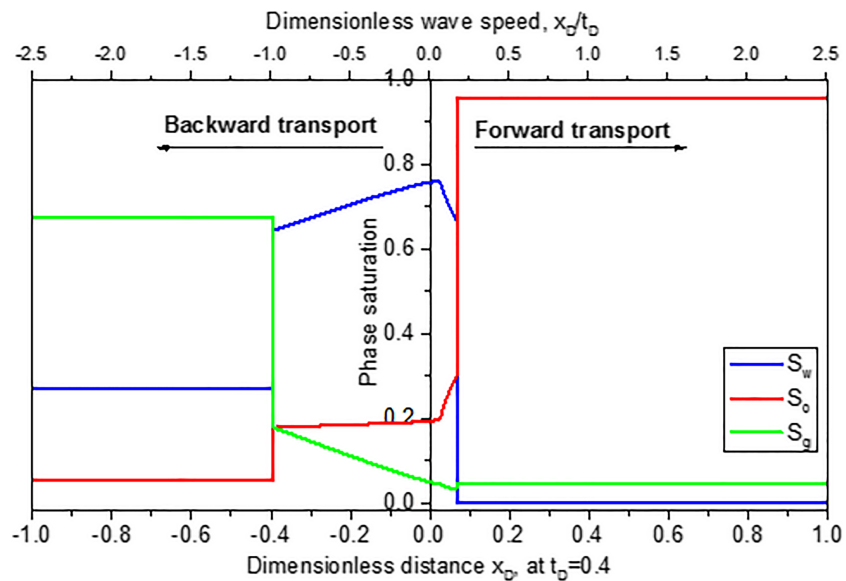
Figure 12. Wave speeds (on the top axis) and saturation profiles (on the bottom axis) for water, oil and gas along the path from J_1 to I_1 in Figures 10 and 11a.

Only the path from J_3 in Figure 11c yields wave speeds that are all positive; state J_3 therefore corresponds to the physical injection condition in Figure 5. J_3, among the multiple possible steady states, is thus the displacing state in Scenario 1 that displaces initial state I_1 outside the foam region.

To illustrate the physical meaning of negative velocities in transport, we illustrate the Riemann solutions in terms of saturation profiles using the path from J_1 in Figure 10. Figure 12 displays the associated wave speeds from Figure 11a as a function of saturations (on the top axis) and also saturations as a function of position at fixed time ($t_D = 0.4$) on the bottom axis. Upon injection, those saturations with positive velocities in Figure 12 move forward from $x_D = 0$, whereas those with negative velocities propagate backward. For $t_D > 0$, the state at $x_D = 0$ is not J_1; thus, the Riemann solution for a displacement with negative wave velocity is physically unacceptable.

4.2. Initial State Inside Foam Region

A similar stability analysis is performed for Scenario 2 for the same set of foam states, J_1, J_2, and J_3 but with a different initial state I_2 now inside the foam region.

Figure 13 illustrates the three composition paths from each of J_1, J_2, and J_3 to I_2, which are solved again based on the definition of equation (15). The structures of the three paths are indicated by their associated tracks: J_1–M_1–I_2; J_2–M_2–I_2; J_3–M_3–I_2. Specifically, the intersection state IJ that splits the slow- and fast-wave groups in the paths corresponds to the points M_1, M_2, and M_3 on Figure 13; these three points are located very close to each other, as seen in the left expanded view of Figure 13, and all belong to the Hugoniot locus of I_2. The paths from J_1 and J_3 to I_2 follow a similar structure, both starting with a slow shock (from J_1 to M_1 or J_3 to M_3) and then reaching I_2 with a fast shock (from M_1 to I_2 or M_3 to I_2). The path from J_2 follows first a spreading wave from J_2 to M_2 and thereafter a shock from M_2 to I_2.

Figures 14a—14c show trajectories of the associated wave speeds as a function of saturations along each path from J_1, J_2, and J_3 to I_2 in dimensionless x_D versus t_D space. Only the path from J_1 to I_2 in the three paths has exclusively trajectories residing in upper quadrant, that is, only positive wave speeds. Therefore, only the strong-foam state, J_1, among the multiple possible injection states, is the physically true displacing state to the initial state I_2.

J_2 is not the displacing state in either scenario. The choice of the displacing state, among the multiple possible injection states, shows a dependence on initial state. In section 4.3, we show the nature of the dependence of the occurrence of J_1 or J_3 on initial state.
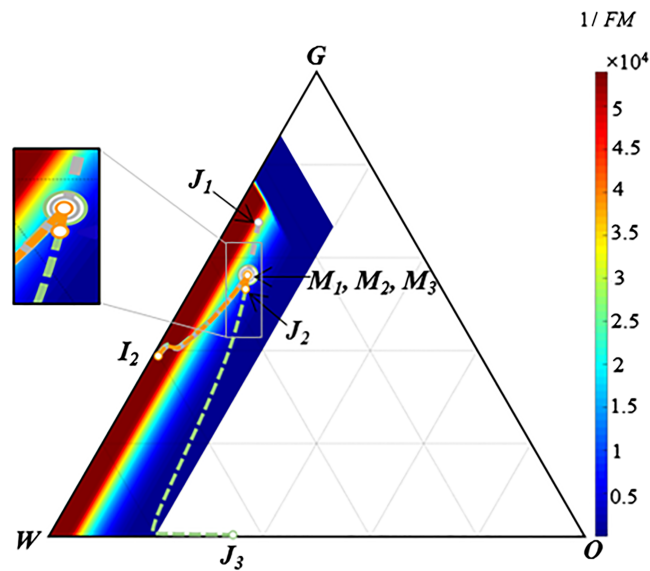
Figure 13. Three composition paths in ternary saturation space constructed from each of J_1, J_2, and J_3, respectively, to I_2 located inside the foam region. The track of each path is: J_1–M_1–I_2; J_2–M_2–I_2; J_3–M_3–I_2. The phase saturations at J_1, J_2, and J_3 are the same as those in Figure 10, fitting the same (f_w, f_o, f_g). A solid curve represents a spreading wave and a dashed curve marks a shock.
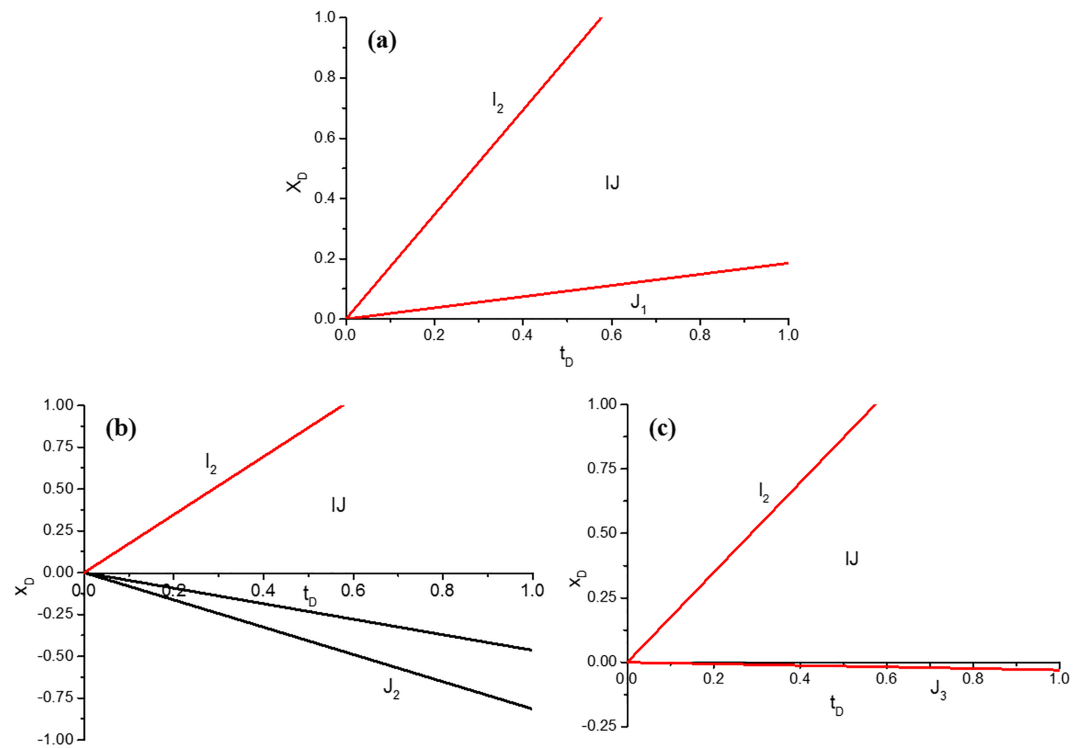

Figure 14. Trajectories of the associated wave speed as a function of saturations along each path from J_1, J_2, and J_3 to I_2 in Figure 13 in dimensionless x_D versus t_D space. A red trajectory marks a shock, with black lines representing characteristics within spreading waves. Only the path from J_1 gives only positive wave speeds.
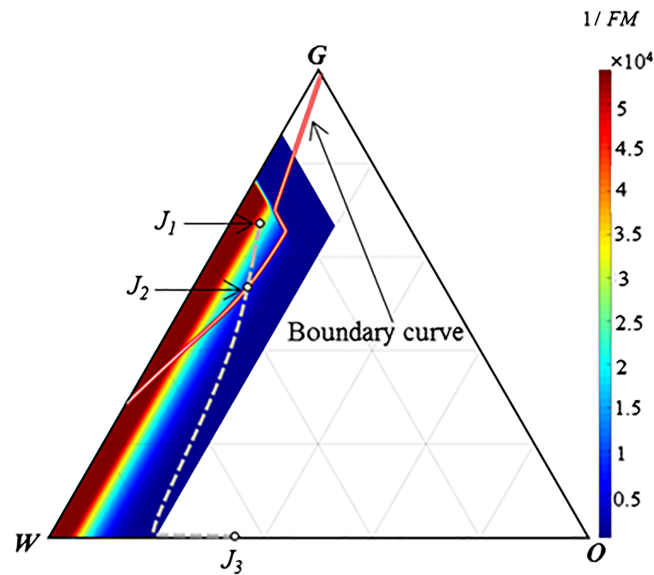
Figure 15. Boundary curve defined through the intermediate state J_2 by equations (18) and (19) that captures the dependence of the nature of the displacement on initial state I.

4.3. Boundary Curve for the Dependence of the Nature of the Displacement on I

To determine which of J_1 or J_3 is the displacing state to any initial state I in ternary saturation space, it is tedious and impractical to go through the calculations as in Figures 11 and 14 for every choice of I. It is then necessary to capture the universal dependence of the choice of the displacing state on initial state in whole ternary saturation space. This is especially crucial to improving the prediction and control of foam displacement with a given initial state in a reservoir, in particular with J corresponding to multiple possible injection states.

Intuitively, for an initial state I_2 inside the foam region, with low S_o favorable for stable foam, it makes sense that strong-foam state J_1, with large μ_{app} and ∇p, would make the displacement. By the same logic, an initial state I_1 outside the foam region, where high S_o kills foam, would be displaced by the collapsed-foam state J_3 with low μ_{app} and ∇p.

However, the location of I inside or outside the foam region is not decisive for the displacement by J_1 or J_3. Instead, ternary saturation space is divided by a "boundary curve" (defined through the intermediate state J_2) that determines which of J_1 or J_3 makes the physically acceptable displacement. Mathematically, the boundary curve is developed in terms of a forward fast-wave curve starting from J_2. Specifically, in the cases presented in this study, its definition is given by the following two conditions:

$$\begin{cases} f_w(S) - f_w(J_2) = \sigma[S_w - S_w(J_2)] \\ f_o(S) - f_o(J_2) = \sigma[S_o - S_o(J_2)] \end{cases}, \tag{18}$$

$$\lambda_f(J_2) > \sigma > \lambda_{s,f}(S), \tag{19}$$

where $\sigma \in R_0^+$, S is a vector of saturations, and subscripts f and s denote the fast and slow eigenvalues of Jacobian matrix in equation (12), respectively. Equation (18) is the expanded form of the Rankine-Hugoniot condition in equation (13). This condition gives all states S along the forward Rankine-Hugoniot locus starting from J_2. Equation (19), as stated in Lax theory (Lax, 1957), defines the 2-Lax shocks starting from J_2. $\lambda_f(J_2)$ in equation (19) is positive, guaranteeing that all admissible 2-Lax shocks from J_2 have positive wave speeds σ. These two conditions therefore in equations (18) and (19) represent a collection of admissible local 2-Lax shocks starting from J_2, illustrated as the boundary curve in Figure 15.

Ternary saturation space as shown in Figure 15 is split into two regions: the region above the boundary curve, where state J_1 resides, and the region below the boundary curve, where state J_3 is located. For any I in the

upper-left region, the strong foam state J_1 is the displacing state that gives a path with wave speeds all positive. In contrast, for any I in the lower-right region, the collapsed-foam state J_3 makes the physically acceptable displacement.

For a state I exactly on the boundary curve in Figure 15, one could not distinguish which of J_1, J_2, or J_3 makes the displacement, since all paths from J_1, J_2, and J_3 are physically admissible in theory. The path from J_2 is connected to I by an admissible 2-Lax shock. Given that J_1, J_2, and J_3 all fit the same injected fractional flows, the path from J_1 or J_3 would jump first to J_2 with zero velocity and then follow the same track as the path from J_2 to I (Castañeda & Furtado, 2016). However, any perturbation that takes I off the boundary curve would always result in negative velocities along any sort of path from J_2, which is physically unacceptable. A physically acceptable displacement would then shift to either J_1 or J_3, depending on the location of I with respect to the boundary curve.

5. Discussion

5.1. Significance for Field Applications

Foam for enhanced oil recovery is of course never co-injected with oil. Nevertheless, geological formations and fluids have many complexities (Lake et al., 2014): geological heterogeneity, fractures, unfavourable mobility ratios of displacing to displaced fluids, gravity segregation, etc. Part of the oil may remain in place due to limited displacement and sweep efficiency after initial gas injection. Since foam enhances greatly the sweep and displacement efficiency of gas injection, it is likely that injected foam flows with oil starting some distance from the well. Direct applications of foam to removing nonaqueous phase liquid contaminants in aquifers and soils would also involve cocurrent foam flow with fluids that may affect foam stability. All these situations may have multiple possible steady states fitting the same injected fractional flows for most process designs. If a displacing phase is a collapsed-foam state, gas-mobility control is much less effective than desired with foam. Negative results include viscous instability and slow displacement and production of oil. The theory and findings presented in this study may assist in predicting the displacing state for given initial conditions. One can then optimize the design of foam processes to ensure their success in engineering applications.

In a simplified one-dimensional model for foam processes in a homogeneous medium, the injected foam lies along the water-gas binary of the phase diagram and the initial state below and to the right. If gas has not previously been injected, the initial state is on the water-oil binary. The foam performance with the particular model parameters we implemented is not sufficiently effective for such a process. Only an initial state I in the small upper-left region in Figure 15 would be displaced by the strong foam state J_1. The poor performance arises in part from the value of the oil parameter *floil* selected, close to S_{or}. This implies that most physically realizable oil saturations destabilize foam somewhat. In addition, in the cases examined foam collapses completely at a modest oil saturation above *fmoil*.

In contrast, experimental observations and field pilots demonstrate that foam can show very good performance in displacing oil (Simjoo & Zitha, 2013; Tang et al., 2018). Thus, the parameters used here for illustration do not by any means represent all foam processes with all oils. By selecting surfactants that enhance foam tolerance to oil, that is, with *floil* well above S_{or} and a large value of *fmoil*, a foam process more resistant to oil could be modeled by techniques similar to those here. Further efforts are needed to explore the displacement behavior with greater tolerance of foam to oil, so that one can represent cases of oil displacement by stronger foam and maximize the benefit of foam applications.

5.2. Experimental Verification of Multiple Steady States

Here we suggest two ways to confirm the multiple steady states predicted for foam flow with oil using laboratory corefloods. First, one could do a displacement, under different initial conditions, with an injection condition (fixed fluxes) that corresponds to multiple steady states. The core would be initialized either at a high S_o such as I_2 or a low S_o like I_1. Foam apparent viscosity or pressure gradient (∇p) achieved at steady state may well depend on the initial conditions. Different foam states achieved for the same injection condition would reflect the existence of multiple steady states, that is, J_1 and J_3. Second, one could fix ∇p and f_g across the core. A series of measurements at steady state with increasing ∇p might give a folding curve similar to Figure 2. Both approaches face challenges. Either of the two approaches needs to start with accurate foam-model

parameters and relative-permeability curves that fit a specific situation. This is time consuming and difficult in the presence of oil, which may require imaging techniques such as X-ray CT to obtain phase-saturation information. Core-scale artifacts (entrance region for foam generation, capillary end effect) can distort core-flood measurements, even at steady state. Moreover, as noted in the wave speeds reported above, the time for foam propagation through a core can be extremely long, especially in the cases of displacement by a weak or collapsed foam.

6. Conclusions

The implicit-texture foam model discussed here predicts multiple steady states for foam flow with oil: an upper strong-foam state J_1, intermediate state J_2, and lower collapsed-foam state J_3, with different apparent viscosities but all fitting same set of fractional flows. A displacement could then correspond to more than one possible injection state for the same injected fractional flows. Our study shows how to determine which state makes the displacement and the dependence of the nature of the displacement on initial condition, using three-phase fractional-flow theory and the wave-curve method.

The WCM for three-phase flow in porous media has a different problem definition than a coreflood with specified injection rates. In a coreflood, injection state J is fixed at, $x_D = 0$ displacing forward initial state I, which is present for $0 < x_D \leq 1$. In the WCM, J is injected from $x_D < \, < 0$, with initial state I present for $x_D > 0$ and J for $x_D \leq 0$.

The distinction between the problem definitions in the WCM and a coreflood makes the WCM capable of identifying the unique displacing state among multiple possible injection states J_1, J_2, and J_3. A composition path, from each of J_1, J_2, and J_3 to initial state I, can be constructed in the WCM, satisfying the conservation equations. Only the path with only positive velocities, in the solutions solved by the WCM, corresponds to a physical injection by J maintained at $x_D = 0$. Any composition path featuring negative velocities does not correspond to this physical injection condition.

A stable displacement could be made by either the upper strong-foam state J_1 or the lower collapsed-foam state J_3, but never the intermediate, intrinsically unstable state J_2. The choice of the displacing state shows a dependence on initial state. We define a boundary curve through the unstable intermediate state J_2 in ternary saturation space that captures the dependence of the nature of the displacement on initial state I. For any I in the region where the upper state J_1 resides, the strong foam state J_1 makes the displacement. For any I located in the region where the lower state J_3 lies, it corresponds to a stable displacement by the collapsed-foam state J_3.

The significance and implications of the findings for field applications are discussed. We also give suggestions for the verification of multiple steady states in foam flow with oil through corefloods in laboratory. Further investigations would account for complexities such as capillary diffusion, formation heterogeneity, and gravity separation in a foam EOR process.

Appendix A: Implicit-Texture Foam Model

The implicit-texture (IT) foam model in the STARS simulator includes two algorithms describing the effect of oil on foam (Computer Modeling Group (Calgary, Alberta, Canada), 2015): the "wet-foam" representation and the "dry-out" representation. The modeling study of Tang et al. (2019) reveals that each of the two representations describes the effect of oil on one foam regime. The wet-foam representation captures the effect of oil only on the low-quality regime, while the dry-out representation depicts the effect of oil on the high-quality regime.

Below is a description of the wet-foam representation implemented in this study. The effect of foam on gas mobility, as defined in the model, is represented through its effect on gas relative permeability, k_{rg}^f. The dry-out representation (Computer Modeling Group (Calgary, Alberta, Canada), 2015; Tang et al., 2019) also predicts a fold in the surface such as in Figure 8. We believe displacements represented by that model would show similar phenomena to those investigated here.

Wet-Foam Representation

Table A1
Model Parameter Values (Using Originally Phase Saturations Not Normalized Saturations) Used for Corey-Type Relative-Permeability and Foam Interpolations

Corey parameters and fluid properties						Foam model parameters		
k_{rw}^o	k_{rg}^o	k_{ro}^o	n_w	n_g	n_o	*fmmob*	*fmdry*	*epdry*
0.20	0.94	0.5	4.2	1.3	2.0	54000	0.316	6000
S_{wc}	S_{gr}	S_{or}	$\mu_w, Pa \cdot s$	$\mu_g, Pa \cdot s$	$\mu_o, Pa \cdot s$	*fmoil*	*floil*	*epoil*
0.2	0.2	0.1	7×10^{-4}	2.07×10^{-5}	5×10^{-3}	0.2	0.12	4

Foam in the STARS model scales gas mobility by modifying k_{rg} in equation (6), the foam-free gas relative permeability, through a mobility-reduction factor *FM*:

$$k_{rg}^f = k_{rg} \cdot FM, \tag{A1}$$

where superscript *f* denotes the presence of foam. k_{rg}^f with foam is usually referred to as effective gas relative permeability. The mobility scaling factor *FM* accounts for the effects of a series of physical factors on foam described by functions F_n ($n = 1, 2, 3 ...$), for example, surfactant concentration, water saturation, oil saturation, capillary number, shear-thinning, or salinity:

$$FM = \frac{1}{1 + fmmob \cdot F_1 \cdot F_2 \cdot F_3 \cdot F_4 \cdot F_5 \cdot F_6 \cdots}, \tag{A2}$$

where *fmmob* is the reference mobility-reduction factor, representing the maximum attainable gas mobility reduction.

This study considers two major factors dominating local-equilibrium foam flow behavior, water (S_w) and oil (S_o) saturations. The effect of S_w is captured through the function F_2:

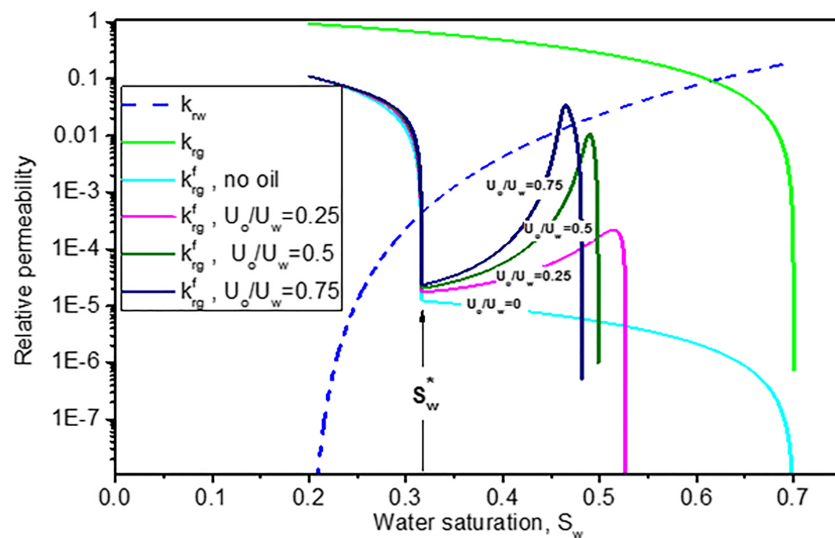$$F_2 = 0.5 + \frac{\arctan[epdry(S_w - fmdry)]}{\pi}, \tag{A3}$$

Figure A1. Gas relative permeability k_{rg}^f with foam, as represented by the wet-foam model. Oil is introduced by fixing various ratios (u_o/u_w), which is equivalent to fixing (f_o/f_w). S_o increases with S_w along each curve at a fixed (u_o/u_w), and the fixed value of S_{gr} corresponds to different values of S_w on the curves, which depend on the values of (u_o/u_w). k_{rw} and k_{rg} are shown for a comparison with k_{rg}^f. All model parameters used for the illustration are in Table A1.

where *fmdry* is the limiting water saturation, physically denoted as S_w^* (Rossen & Zhou, 1995), the water saturation around which foam collapses. Parameter *epdry* determines the abruptness of foam collapse in a narrow range of S_w around *fmdry*. In the wet-foam model, *fmdry* is a fixed constant.

Oil here does not have an impact on foam stability (i.e., on *fmdry*), which dominates the high-quality regime. It affects foam only in the low-quality regime, through its effect on *fmmob*:

$$F_3 = \begin{cases} 1 & S_{or} \leq S_o \leq floil \\ \left(\dfrac{fmoil - S_o}{fmoil - floil} \right)^{epoil} & floil \leq S_o \leq fmoil \\ 0 & fmoil \leq S_o \leq 1 - S_{wc} - S_{gr} \end{cases}, \qquad (A4)$$

where S_{wc}, S_{or}, and S_{gr} represent the residual saturations of water, oil, and gas, respectively. Equation (A4) is a piecewise smooth function depicting the effect of S_o through three factors *fmoil*, *floil*, and *epoil*. The factors *fmoil* and *floil* denote the upper- and lower-limiting values of S_o for stable foam. For $S_o > fmoil$, foam is killed completely ($F_3 = 0$). For S_o less than *floil*, oil has no effect on foam ($F_3 = 1$). For $floil < S_o < fmoil$, oil destabilizes foam in a nonlinear way.

Table A1 summarizes the model parameters implemented throughout the study. Note that all of our illustrations in ternary diagrams, that is, Figures 7, 9, 10, 13, and 15, are plotted using normalized saturations rescaled as follows:

$$S_j = \frac{S_{j,a} - S_{jr}}{1 - S_{wc} - S_{or} - S_{gr}}, \qquad (A5)$$

where $S_{j,a}$ with subscript a denotes the absolute saturation of phase j and S_{jr} represents the residual saturation of phase j. Residual saturations of phase j, that is, S_{wc}, S_{or}, and S_{gr}, are not shown in the illustrations.

Figure A1 illustrates gas relative-permeability curves on semi-log scale using parameters in Table A1, as described by the wet-foam representation above. Without foam, k_{rg} (green curve) is much greater than k_{rw} (dashed blue curve) for a wide range of S_w, indicating a large gas mobility that is usually unfavourable for oil displacements. With foam but without oil, k_{rg}^f (cyan curve) drops down suddenly and drastically, by a factor of 10^4, within a narrow range of S_w around *fmdry*. The abruptness of the drop depends on the value of *epdry* in equation (A3).

In Figure A1, the effect of oil is introduced by fixing the ratio (u_o/u_w), equivalent to fixing (f_o/f_w). Note that parameter *fmdry*, around which k_{rg}^f drops abruptly and suddenly, remains independent of the presence of oil and of (u_o/u_w). The unchanging value of *fmdry* reflects the fact that the wet-foam representation describes the effect of oil only on the low-quality regime. For $S_w > fmdry$, increasing the ratio (u_o/u_w) at fixed S_w raises S_o, as seen from equations (4) and (6). That means increasingly weaker foam (smaller value of F_3 in equation (A4)), causing k_{rg}^f in Figure A1 to increase nonlinearly. As S_o increases enough to kill foam, k_{rg}^f rises largely, because gas mobility is no longer restricted by foam. k_{rg}^f thereafter drops drastically down to zero as S_g approaches its residual saturation.

References

Adebayo, A. R. (2018). Viability of foam to enhance capillary trapping of CO₂ in saline aquifers—An experimental investigation. *International Journal of Greenhouse Gas Control*, 78, 117–124.

Adebayo, A. R. (2019). Measurements of capillary pressure and relative permeability curves for foam transport in porous media—A capillary bundle approach. *Journal of Petroleum Science and Engineering*, 172, 1048–1056.

Afsharpoor, A., Lee, G. S., & Kam, S. I. (2010). Mechanistic Simulation of continuous gas injection period during surfactant-alternating-gas (SAG) processes using foam catastrophe theory. *Chemical Engineering Science*, 65(11), 3615–3631. https://doi.org/10.1016/j.ces.2010.03.001

Al Ayesh, A. H., Salazar, R., Farajzadeh, R., Vincent-Bonnieu, S., & Rossen, W. R. (2017). Foam diversion in heterogeneous reservoirs: Effect of permeability and injection method. *SPE Journal* SPE-179650-PA, 22(5), 1402–1415. https://doi.org/10.2118/179650-PA

Alcorn, Z. P., Fredriksen, S. B., Sharma, M., Rognmo, A. U., Føyen, T. L., Fernø, M. A., & Graue, A. (2018). An integrated CO₂ foam EOR pilot program with combined CCUS in an onshore Texas heterogeneous carbonate field. In SPE Improved Oil Recovery Conference. Society of Petroleum Engineers.

Alvarez, J. M., Rivas, H. J., & Rossen, W. R. (2001). Unified model for steady-state foam behavior at high and low foam qualities. SPE-74141-PA. https://doi.org/10.2118/74141-PA.

Arnold, V. I., Kazarinoff, N., Afrajmovich, V. S., Il'yashenko, Y. S., & Shil'nikov, L. P. (1999). *Dynamical systems V: Bifurcation theory and catastrophe theory*. Berlin Heidelberg: Springer. Retrieved from https://books.google.nl/books?id=orhzQgAACAAJ

Avraam, D., & Payatakes, A. (1995). Flow regimes and relative permeabilities during steady-state two-phase flow in porous media. *Journal of Fluid Mechanics*, *293*, 207–236. https://doi.org/10.1017/S0022112095001698

Azevedo, A. V., de Souza, A. J., Furtado, F., Marchesin, D., & Plohr, B. (2010). The solution by the wave curve method of three-phase flow in virgin reservoirs. *Transport in Porous Media*, *83*(1), 99–125.

Boeije, C. S., & Rossen, W. (2015). Fitting foam-simulation-model parameters to data: I. Coinjection of gas and liquid. SPE-174544-PA. https://doi.org/10.2118/174544-PA273-284).

Buckley, S. E., & Leverett, M. C. (1942). Mechanism of fluid displacement in sands. *Transactions of AIME*, SPE-942107-G, *146*(1), 107–116. https://doi.org/10.2118/942107-G

Castañeda, P. (2018). Explicit construction of effective flux functions for Riemann solutions. In C. Klingenberg, & M. Westdickenberg (Eds.), *Theory, numerics and applications of hyperbolic problems I. HYP 2016. Presented at the XVI International Conference on Hyperbolic Problems: Theory,* Numerics, Applications (pp. 273–284). Cham: Springer.

Castañeda, P., Abreu, E., Furtado, F., & Marchesin, D. (2016). On a universal structure for immiscible three-phase flow in virgin reservoirs. *Computational Geosciences*, *20*(1), 171–185.

Castañeda, P., & Furtado, F. (2016). The role of sonic shocks between two-and three-phase states in porous media. *Bulletin of the Brazilian Mathematical Society, New Series*, *47*(1), 227–240.

Chalbaud, C. A., Moreno, R. A., & Alvarez, J. M. (2002). Simulating foam process for a Venezuelan pilot test. Society of Petroleum Engineers. https://doi.org/10.2118/77699-MS

Charbeneau, R. J. (1988). Multicomponent exchange and subsurface solute transport: Characteristics, Coherence, and the riemann problem. *Water Resources Research*, *24*(1), 57–64.

Cheng, L., Reme, A. B., Shan, D., Coombe, D. A., & Rossen, W. R. (2000). Simulating foam processes at high and low foam qualities. (2000) SPE-59287-MS. SPE: Society of Petroleum Engineers. https://doi.org/10.2118/59287-MS

Computer Modeling Group (Calgary, Alberta, Canada)*, STARS User's Guide,* Version 2015*,* See also *GEM User's Guide,* Version 2015.

Farajzadeh, R., Andrianov, A., Krastev, R., Hirasaki, G. J., & Rossen, W. R. (2012). Foam-oil interaction in porous media: Implications for foam assisted enhanced oil recovery. *Advances in Colloid and Interface Science*, *183–184*, 1–13. https://doi.org/10.1016/j.cis.2012.07.002

Gauglitz, P. A., Friedmann, F., Kam, S. I., & Rossen, W. R. (2002). Foam generation in homogeneous porous media. *Chemical Engineering Science*, *57*(19), 4037–4052. https://doi.org/10.1016/S0009-2509(02)00340-8

Geistlinger, H., Detlef, L., Gunnar, K., & Hans-Jörg, V. (2009). Pore-scale and continuum modeling of gas flow pattern obtained by high-resolution optical bench-scale experiments. *Water Resources Research*, *45*, W04423. https://doi.org/10.1029/2007WR006548

Golubitsky, M., & Keyfitz, B. L. (1980). A qualitative study of the steady-state solutions for a continuous flow stirred tank chemical reactor. *SIAM Journal on Mathematical Analysis*, *11*(2), 316–339.

Guckenheimer, J. (1986). Multiple bifurcation problems for chemical reactors. *Physica D: Nonlinear Phenomena*, *20*(1), 1–20.

Holmes, P., & Rand, D. (1976). The bifurcations of Duffings equation: An application of catastrophe theory. *Journal of Sound and Vibration*, *44*(2), 237–253.

Iglauer, S., Paluszny, A., Pentland, C. H., & Blunt, M. J. (2011). Residual CO_2 Imaged with X-ray micro-tomography. *Geophysical Research Letters*, *38*, L21403. https://doi.org/10.1029/2011GL049680

Iglauer, S., Wülling, W., Pentland, C. H., Al-Mansoori, S. K., & Blunt, M. J. (2011). Capillary-trapping capacity of sandstones and sandpacks. *SPE Journal*, *16*(04), 778–783.

Jeong, S.-W., & Corapcioglu, M. Y. (2005). Force analysis and visualization of NAPL removal during surfactant-related floods in a porous medium. *Journal of Hazardous Materials*, *126*(1), 8–13.

Johnson, P. C., Johnson, R. L., Bruce, C. L., & Leeson, A. (2001). Advances in in situ air sparging/biosparging. *Bioremediation Journal*, *5*(4), 251–266. https://doi.org/10.1080/20018891079311

Juanes, R., Spiteri, E. J., Orr, F. M., & Blunt, M. J. (2006). Impact of relative permeability hysteresis on geological CO_2 storage. *Water Resources Research*, *42*, W12418. https://doi.org/10.1029/2005WR004806

Kam, S. I., Nguyen, Q. P., Li, Q., & Rossen, W. R. (2007). Dynamic simulations with an improved model for foam generation. *SPE Journal*, *12*(01), 35–48.

Kam, S. I., & Rossen, W. R. (2003). A model for foam generation in homogeneous media. SPE-87334-PA. https://doi.org/10.2118/87334-PA

Kao, C. M., Chen, C. Y., Chen, S. C., Chien, H. Y., & Chen, Y. L. (2008). Application of in situ biosparging to remediate a petroleum-hydrocarbon spill site: Field and microbial evaluation. *Chemosphere*, *70*(8), 1492–1499. https://doi.org/10.1016/j.chemosphere.2007.08.029

Khatib, Z. I., Hirasaki, G. J., & Falls, A. H. (1988). Effects of capillary pressure on coalescence and phase mobilities in foams flowing through porous media. *SPE Reservoir Engineering*, *3*(03), 919–926.

Kim, J., Dong, Y., & Rossen, W. R. (2005). Steady-state flow behavior of CO2 foam. SPE-89351-PA. https://doi.org/10.2118/89351-PA.

Kovscek, A. R., Chen, Q., & Gerritsen, M. (2010). Modeling foam displacement with the local-equilibrium approximation: Theory and experimental verification. *SPE Journal*, *15*(1), 171–183.

Kovscek, A. R., Patzek, T. W., & Radke, C. J. (1995). A mechanistic population balance model for transient and steady-state foam flow in boise sandstone. *Chemical Engineering Science*, *50*(23), 3783–3799. https://doi.org/10.1016/0009-2509(95)00199-F

Kovscek, A. R., Tadeusz, W. P., & Radke, C. J. (1997). Mechanistic foam flow simulation in heterogeneous and multidimensional porous media. *SPE Journal*, *2*(4), 511–526.

Kravtsov, Y. A., & Orlov, Y. I. (1990). *Geometrical optics of inhomogeneous media: Springer series on wave phenomena*. New York: Springer-Verlag, Inc.

Lake, L. W., Johns, R. T., Rossen, W. R., & Pope, G. (2014). *Fundamentals of enhanced oil recovery*. Richard, TX: Society of Petroleum Engineers.

Lax, P. D. (1957). Hyperbolic systems of conservation laws II. *Communications on Pure and Applied Mathematics*, *10*(4), 537–566.

Li, R. F., Yan, W., Liu, S., Hirasaki, G., & Miller, C. A. (2010). Foam mobility control for surfactant enhanced oil recovery. *SPE Journal*, *15*(4), 928–942.

Liu, T. P. (1974). The Riemann problem for general 2×2 conservation laws. *Transactions of the American Mathematical Society*, *199*, 89–112.

Lotfollahi, M., Farajzadeh, R., Delshad, M., Varavei, A., & Rossen, W. R. (2016). Comparison of implicit-texture and population-balance foam models. *Journal of Natural Gas Science and Engineering*, *31*, 184–197.

Ma, K., Lopez-Salinas, J. L., Puerto, M. C., Miller, C. A., Biswal, S. L., & Hirasaki, G. J. (2013). Estimation of parameters for the simulation of foam flow through porous media. Part 1: The dry-out effect. *Energy & Fuels*, *27*(5), 2363–2375.

Ma, K., Mateen, K., Ren, G., Luo, H., Bourdarot, G., & Morel, D. (2018). Mechanistic modeling of foam flow through porous media in the presence of oil: Review of foam-oil interactions and an improved bubble population-balance model. Presented at the SPE Annual Technical Conference and Exhibition, Society of Petroleum Engineers.

Myers, T. J., & Radke, C. J. (2000). Transient foam displacement in the presence of residual oil: Experiment and simulation using a population-balance model. *Industrial & Engineering Chemistry Research*, *39*(8), 2725–2741. https://doi.org/10.1021/ie990909u

Namdar Zanganeh, M., Kam, S. I., LaForce, T., & Rossen, W. R. (2011). The method of characteristics applied to oil displacement by foam. SPE-121580-PA. https://doi.org/10.2118/121580-PA.

Norris, S. O., Scherlin, J. M., Mukherjee, J., Vanderwaal, P., Abbas, S., & Nguyen, Q. P. (2014). CO_2 foam pilot in Salt Creek Field, Natrona County, WY: Phase II: Diagnostic testing and initial results. Society of Petroleum Engineers. https://doi.org/10.2118/170729-MS

Purohit, P. K., & Bhattacharya, K. (2003). Dynamics of strings made of phase-transforming materials. *Journal of the Mechanics and Physics of Solids*, *51*(3), 393–424. https://doi.org/10.1016/S0022-5096(02)00097-2

Reynolds, C., & Krevor, S. (2015). Characterizing flow behavior for gas injection: Relative permeability of CO_2-brine and N_2-water in heterogeneous rocks. *Water Resources Research*, *51*, 9464–9489. https://doi.org/10.1002/2015WR018046

Rognmo, A. U., Fredriksen, S. B., Alcorn, Z. P., Sharma, M., Føyen, T., Eide, Ø., & Fernø, M. (2018). Pore-to-core EOR upscaling for CO2-foam for CCUS. In SPE Europec featured at 80th EAGE Conference and Exhibition. Society of Petroleum Engineers.

Rossen, W. R. (1996). Foams in enhanced oil recovery. In *foams: Theory, measurements, and applications* (pp. 413–464). New York: MaRcel Dekker. https://doi.org/10.1002/food.19970410116

Rossen, W. R. (2013). Numerical challenges in foam simulation: A review. SPE-166232-MS. SPE: Society of Petroleum Engineers. https://doi.org/10.2118/166232-MS.

Rossen, W. R., & Zhou, Z. H. (1995). Modeling Foam Mobility at the Limiting Capillary Pressure. *SPE Advanced Technology Series*, *3*, 146–152.

Schramm, L. L. (1994). Foams: Fundamentals and applications in the petroleum industry. In C. M. Joan (Ed.), *Foams: Fundamentals and Applications in the Petroleum Industry* (Vol. 242, pp. i–vii). Washington, DC: American Chemical Society. https://doi.org/10.1021/ba-1994-0242.fw001

Shah, S. Y., Wolf, K.-H., Pilus, R. M., & Rossen, W. R. (2018). Foam generation by capillary snap-off in flow across a sharp permeability transition. SPE Journal.

Sharma, M., Alcorn, Z. P., Fredriksen, S., Fernø, M., & Graue, A. (2017). Numerical modelling study for designing CO2-foam field pilot. In IOR 2017-19th European Symposium on Improved Oil Recovery.

Simjoo, M., Dong, Y., Andrianov, A., Talanana, M., & Zitha, P. (2013). CT scan study of immiscible foam flow in porous media for enhancing oil recovery. *Industrial & Engineering Chemistry Research*, *52*(18), 6221–6233.

Simjoo, M., & Zitha, P. L. J. (2013). Effects of oil on foam generation and propagation in porous media. SPE-165271-MS. https://doi.org/10.2118/165271-MS.

Smoller, J. (2012). *Shock waves and reaction-diffusion equations* (Vol. 258). New York: Springer Science & Business Media.

Spirov, P., Rudyk, S., & Khan, A. (2012). Foam assisted WAG, Snorre revisit with new foam screening model. Society of Petroleum Engineers. https://doi.org/10.2118/150829-MS

Stone, H. (1970). Probability model for estimating three-phase relative permeability. *Journal of Petroleum Technology*, *22*(2), 214–218.

Stone, H. (1973). Estimation of three-phase relative permeability and residual oil data. *Journal of Canadian Petroleum Technology*, *12*(4).

Tang, J. (2019). The effect of oil on foam for enhanced oil recovery: Theory and measurements. PhD dissertation at Delft University of Technology, Netherlands. https://doi.org/10.4233/uuid:49763197-fec0-49e6-a496-6ac0068585db.

Tang, J., Ansari, M. N., & Rossen, W. R. (2019). Quantitative modeling of the effect of oil on foam for enhanced oil recovery. *SPE Journal*, *24*(03), 1057–1075.

Tang, J., Vincent-Bonnieu, S., & Rossen, W. (2019). Experimental investigation of the effect of oil on steady-state foam flow in porous media. *SPE Journal*, *24*(01), 140–157.

Thom, R., & Zeeman, E. (1974). Catastrophe theory: Its present state and future perspectives. *Dynamical Systems-Warwick*, *468*, 366.

Vitoonkijvanich, S., AlSofi, A. M., & Blunt, M. J. (2015). Design of foam-assisted carbon dioxide storage in a North Sea aquifer using streamline-based simulation. *International Journal of Greenhouse Gas Control*, *33*, 113–121.

Wiggins, S. (2013). *Global bifurcations and chaos: Analytical methods*. New York. Springer. Retrieved from https://books.google.nl/books?id=s1zdBwAAQBAJ

Wooding, R., & Morel-Seytoux, H. J. (1976). Multiphase fluid flow through porous media. *Annual Review of Fluid Mechanics*, *8*(1), 233–274.

Zeeman, E. C. (1977). *Catastrophe Theory: Selected papers* (pp. 1972–1977). Boston: Addison-Wesley.